Chemical Science

ROYAL SOCIETY OF CHEMISTRY

EDGE ARTICLE

View Article Online
View Journal | View Issue

Cite this: *Chem. Sci.*, 2026, **17**, 3525

All publication charges for this article have been paid for by the Royal Society of Chemistry

Received 4th November 2025
Accepted 21st December 2025

DOI: 10.1039/d5sc08536e

rsc.li/chemical-science

Robust Janus-faced quasi-solid-state honeycomb-mimicking electrolytes for the fast transport and adequate supply of sodium ions

Fang Chen,[a] Yadan Xie,[a] Zhoubin Yu,[a] Na Li,[a] Yu Qiao *[b] and Xiang Ding *[c]

Quasi-solid-state electrolytes are one of the most promising alternative candidates for traditional liquid state electrolytes with a fast ion transport rate, high mechanical strength and wide temperature adaptation. Here, we have designed a biomimicking electrolyte film with a Janus-faced honeycomb-like structure and applied it to sodium ion batteries. The advanced quasi-solid-state sodium ion batteries show an initial coulombic efficiency of 105% and stable charge–discharge cycles over a wide temperature range from −20 °C to 60 °C. Additionally, *operando* observations of the chemical structure and interfacial evolution have been carried out, demonstrating a robust and stable quasi-solid-state electrolyte film.

Introduction

A revolution, moving from traditional liquid electrolytes to quasi-solid-state electrolytes and then to all-solid-state electrolytes, is underway for alkali metal ion batteries that aim to push beyond the limits of energy density.[1–4] Quasi-solid-state electrolytes (QSSE), namely gel electrolytes, have been considered to be one of the most promising candidates for next-generation rechargeable batteries based on their tremendous chemical, mechanical and electrochemical merits. QSSEs have improved mechanical flexibility, alleviated solution leakage, enhanced cycling stability, and extended working potential window, among other merits, as compared to liquid electrolytes.[5–7] In contrast to all-solid-state electrolytes, gel electrolytes address issues like poor interfacial contact, high operating temperature, relatively low room-temperature conductivity, *etc.*[8,9] Moreover, QSSEs with a polymer matrix are expected to demonstrate more functionalities and possibilities than those with merely assisted ion transport with ingenious design.[10,11] For instance, gel electrolytes with flexibility, widened operating temperature and safety insurance have been developed and applied for lithium ion batteries (LIBs). Nevertheless, as a potential alternative to LIBs, sodium ion batteries (SIBs) with multi-functional QSSEs have remained an underdeveloped project and further exploration of their possibilities is needed.[12–14]

Although research on SIBs dates back to 1960s, similarly to LIBs (1970s), practical problems remain to be solved and their electrochemical properties have yet to be perfected.[15,16] For instance, the thermodynamics and kinetics of the growth of sodium dendrites are not yet fully understood, since they differ greatly from lithium dendrites.[17] These sodium dendrites can trigger severe damage to cells by consuming electrolytes, increasing impedance and even worse, penetrating the separators, which leads to short circuits. According to previous research,[18–21] sodium dendrites have higher plastic compliance and more unstable SEI growth than lithium dendrites. Therefore, it is necessary to suppress the growth of sodium dendrites to obtain stable and safe SIBs.[22] Strategies that involve optimized electrolytes and interfacial engineering have been proposed. An electrode–electrolyte interface with enhanced mechanical strength to prevent dendrites has been confirmed to be effective and efficient.[23] On the cathode side, the trade-off between high capacity and stable cycling performance creates complications. Taking Prussian blue analogues (PBAs), *e.g.*, $Na_{2-x}Fe[Fe(CN)_6]$, as an example, their theoretical specific capacity of 171 mAh g^{-1} ($x = 0$) is high, but their current reversible capacity is often below 120 mAh g^{-1} owing to sodium deficiency. Sodium deficiency also affects cycling stability, because high sodium contents correspond to a rhombohedral crystal structure, which has higher structural stability through charge–discharge cycles than a cubic phase.[24,25] Modifications to the fabrication process are the most popular way to synthesize PBAs with a sufficient proportion of Na, but require delicate operation or the inappropriate wastage of raw materials.[26] Gel electrolytes have been considered as an option for broadening the temperature range and achieving fire resistance for sodium ion batteries. For thermal stability, Xiu-Li Wang and his coworkers incorporated diethyl vinylphosphonate (DEVP) into

[a]*Zhejiang Baima Lake Laboratory Co., Ltd, 310052 Hangzhou, Zhejiang, China*
[b]*State Key Laboratory of Physical Chemistry of Solid Surfaces, Discipline of Intelligent Instrument and Equipment, College of Chemistry and Chemical Engineering, Xiamen University, Xiamen 361005, China. E-mail: yuqiao@xmu.edu.cn*
[c]*College of Chemistry and Materials Science, Fujian Key Laboratory of Polymer Materials, Fujian Normal University, Fuzhou, 350007, China. E-mail: dingx@fjnu.edu.cn*

a PAN polymer matrix for high temperature stability; the film can sustain its shape when the temperature rises to 180 °C.[27] Additionally, phosphorus and fluorine are used to extinguish fire and inhibit its further spread in polymer electrolytes, and agents such as tri(acryloyloxyethyl) phosphate (TAEP) have proven to be efficient.[28]

Herein, we propose a multi-functional gel electrolyte with a Janus-faced structure fabricated *via* phase inversion, with one 'face' to suppress sodium dendrites and another to supply sodium ions and buffer free electrolytes. As a high-performance QSSE, its microscopic structure should have abundant cavities to store electrolyte solution and densely arranged shared walls to resist external stress. The synthesized QSSE film features a spontaneously formed morphology that resembles natural honeycomb and consequently attains high flexibility and plasticity. To support as much honey and pollen as possible, as well as to sustain integrity, natural honeycomb has aligned hives with shared sides for bees to work on and brood in. The honeycomb-like Janus-faced (HJ) QSSE has been introduced into sodium ion batteries and exhibits a sodium-ion diffusion rate comparable to that of liquid electrolytes. The HJ film has demonstrated outstanding thermal stability (maintaining its shape at 300 °C) and self-extinguishing ability. The assembled quasi-solid-state sodium ion batteries demonstrate a superior sodium storage capability with an initial capacity of 130 mAh g^{-1}, 90% capacity retention after 700 charge–discharge cycles and robust charge–discharge performance over a wide temperature range. Additionally, assisted by *operando* tests, the stability of the crystal chemical structures and interfacial properties have been demonstrated.

Experimental section

Synthesis of HJ film

Poly(vinylidene fluoride-*co*-hexafluoropropylene) (PVDF-HFP), average M_w: 40 000, pellets, was purchased from Shanghai Macklin Biochemical Technology Co., Ltd ZSM-5 molecular sieves were obtained from SINOPEC Shanghai research institute of petrochemical technology Co., Ltd, as a powder. 1-Methyl-2-pyrrolidinone (NMP), >99.0%, was purchased from Shanghai Macklin Biochemical Technology Co., Ltd.

(1) Preparation of 10% PVDF-HFP solution. First, 2 g PVDF-HFP and 18 g NMP were added to a glass bottle with a magneton, and the solution was stirred at room temperature until full dissolution occurred (~4 h).

(2) Preparation of the precursor solution. A certain amount of ZSM-5 was added to the above-mentioned solution. The amount of ZSM-5 varied from 3 g (PVDF-HFP : ZSM-5 = 4 : 6) to 4.7 g (PVDF-HFP : ZSM-5 = 3 : 7) according to our experimental results. The ratio of PVDF-HFP : ZSM-5 can be deceased to 1 : 9 with the addition of extra NMP.

(3) Preparation of HJ film. First, the surface of a piece of glass (20 × 8 cm^2) was covered with the solution with the aid of a scraper. The thickness of the scraper was 100 μm; this was increased to 1000 μm to for the *operando* optical microscopy experiment. The glass was then placed into a container filled with 600 mL deionized water and left there for 6 h for solution exchange at room temperature. The film was then taken out and placed in an oven for drying at 110 °C for 24 h with vacuum pumping.

Synthesis of PBA cathode

The synthesis process for the PBA powders followed a co-precipitation method detailed in a previously reported article.[29] The PBA powders were then mixed with super P and PVDF in a ratio of 8 : 1 : 1 with certain amount of NMP. The slurry was scraped on an Al foil with a thickness of 100 μm. The film was dried at 80 °C in an oven with vacuum pumping, and the cathode film was then cut into appropriate sizes as needed.

Characterization

The crystal structure of the materials was determined using a D8 ADVANCE X-ray diffractometer with a Cu Kα radiation line ($\lambda = 1.5418$ Å). SEM images were taken using an SEM5000X from Chinainstru & Quantumtech (Hefei) Co., Ltd. The TGA analysis was carried out using an Sdt Q600 V20 9 Build 20 Thermal Gravimetric Analyzer with a scanning rate of 10 °C min^{-1}.

Electrochemical test

A quasi-solid-state cell was assembled with a piece of cathode film, HJ film swollen with liquid electrolytes (1 M $NaClO_4$ in PC/EC/FEC: 45 : 45 : 10) and sodium metal foil. The control sample was assembled with the HJ film replaced with glass fiber (GF). The galvanostatic charge–discharge experiments were carried out in a LAND CT3002A multichannel battery test system. The cyclic voltammetry (CV) tests (potential window: 2–4 V) and electrochemical impedance spectroscopy (EIS, 10^{-2} Hz to 10^5 Hz with an amplitude of 5 mV) were operated using a CHI 660E workstation. The *operando* optical microscopy experiment was carried out with an *Operando* Confocal Microscopy assisted with a LAND CT3002A.

Results and discussion

In QSSEs, the electrolyte solution can exist in different forms, either swollen by polymers or filling microscopic pores. Consequently, a higher porosity translates into a larger electrolyte uptake.[30] A porous structure with regular aligned pores can sustain external compression. Conversely, a dense structure with fewer pores leads to less contact between the liquid electrolyte solution with the electrode, but at the same time, fewer side effects. Therefore, the trade-off between the proportion and distribution of microscopic pores is challenging, yet of importance. In this work, a phase inversion process was utilized to fabricate an asymmetric membrane consisting of a polymer-rich skin layer and a polymer-lean porous sub-layer that combine high mechanical strength with excellent electrochemical performance.

The synthesis process is depicted in Fig. 1a. A solution containing polymers, molecular sieves and the solvent (NMP) was cast on a glass plate and placed in a container with a non-solvent to initiate a solvent (DI water) exchange process. The membrane formation process is displayed in the ternary phase

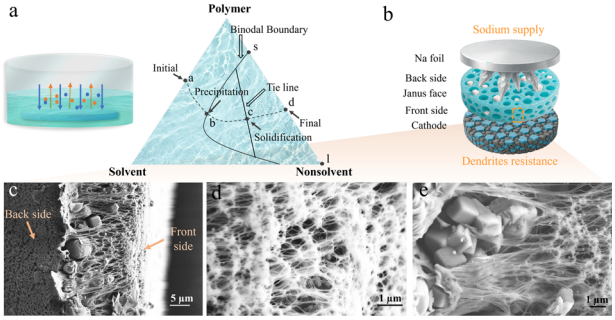

Fig. 1 Schematic illustration of (a) the synthesis process of the HJ film and (b) a cell with a Janus-faced gel electrolyte. Microscopic images of a cross-sectional view of (c) the entire section, (d) the front side and (e) the back side.

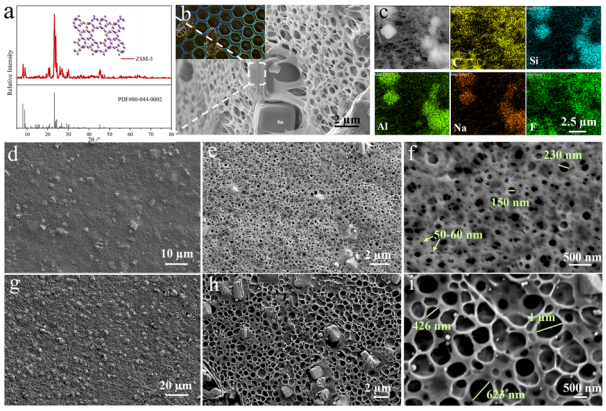

Fig. 2 (a) XRD pattern of ZSM-5 molecular sieves. (b) SEM images of the honeycomb-like structure, inset image: natural honeycomb. (c) Elemental mapping of the HJ film. (d–f) Front-side view of the HJ film at different magnifications. (g–i) Back-side view of the HJ film at different magnifications.

diagram on the right side in Fig. 1a, and the dashed line abcd describes the evolution progress of the system. After being placed into the non-solvent, an instant solution exchange takes place, and a thin-skin layer is formed. The binodal boundary line divides the diagram into a single-phase region and a binary-phase region. Thus, a transformation takes place at point b, and the system breaks into two phases, *i.e.*, the polymer-rich phase and polymer-lean phase, which finally evolve into the membrane matrix and the pore regions, respectively. This is because solvent exchange is rapid at the film surface but sluggish in the bulk. The separation process is completed at point c. The final point d represents the final composition of the system with a certain ratio of the membrane part (represented by the point s) and pore part (represented by the point l). Moreover, with the phase inversion process, the molecular sieves, which have the highest hardness in the system, precipitate and gather at the bottom, creating a concentration gradient from the bottom to the top. After the non-solvent is removed, the membrane shows a distinct morphology with a dense front side, a hard back side and a porous inner layer in between. The optical images in Fig. S1 show that the HJ film becomes semi-transparent after being swollen with the electrolyte solution. The surface also exhibits a typical Turing pattern. A quasi-solid-state sodium ion cell was assembled with the back side of the HJ gel electrolytes facing the sodium metal and the front side facing the cathode, as displayed in Fig. 1b. The cross-section area was magnified and is shown in the SEM images in Fig. 1c–e. The cross-section area presents a sponge-like porous structure, which should accommodate the electrolyte solution and resist compression. The inorganic particles clustered on the back side owing to gravity, and this dense layer could resist sodium metal dendrite penetration, functioning as a safety mechanism. The structure is relatively dense on the front side to minimize electrolyte contact with the cathode, suppressing side reactions and extending cycle life.

The chemical structures, microstructures and physical properties of synthesized HJ film were characterized. As shown in Fig. 2a, the molecular sieves (ZSM-5) in the film were indexed to a tetragonal phase, with the space group $P4_22_12$, as identified using the standard diffraction pattern JCPDS#00-044-000. The cations present in this molecular structure are sodium ions, thus supplying extra sodium ions for the sodium ion batteries. Moreover, ZSM-5 is a 5 Å-type molecular sieve, providing channels with a radius of ~0.5 nm, which is sufficient for solvated sodium ions (Stokes radius for Na^+: ~4.6) to pass through. In contrast, the XRD pattern of a piece of HJ film exhibits an extra broad peak from 15° to 30° (Fig. S2), showing that the PVDF-HFP has an amorphous phase in the film. The thermostability of the HJ film (Fig. S3a) and a piece of commercialized PE separator (Fig. S3b) were tested and compared *via* thermal analysis. The decomposition temperature increased to 440 °C for the HJ film compared to 260 °C for the PE film, indicating a significant improvement for the HJ film. Beyond 600 °C, the PE film was completely decomposed, while only PVDF-HFP part of the HJ film was decomposed and the remaining part (molecular sieve) could survive the high temperature.

As displayed in Fig. 2b, the microstructure of the HJ film resembles the pore alignment of honeycomb, which is constructed using less material and has higher porosity and high strength. Owing to its structural superiority, the HJ film is able to lift a heavy load more than 2000 times its own weight, as shown in Fig. S4. Additionally, the film is bendable and stretchable (Fig. S5). Fig. 2c reveals the distribution of the elements C, Si, Al, Na and F on the surface of a piece of HJ film. ZSM-5 contains the elements C (absorbed organics), Si and F, while PVDF-HFP contains the element C and F, corresponding to the mapping results. The two faces of the HJ film show different morphologies, as demonstrated *via* comparison of the SEM images of the front side (Fig. 2d–f) and back side (Fig. 2g–i) at different magnifications. As clearly seen from Fig. 2d and g, there are more molecular sieve particles at the back side than the front side from the overall view, as verified in Fig. 2e and h. Different kinds of pore distributions are clearly exhibited in Fig. 2f and i, demonstrating the distinctive features of the skin layer and sponge layer. On the front side, the pores generally have a diameter of less than 300 nm, with most around 100 nm, showing a dense structure. In contrast, most pores have

diameters of greater than 400 nm on the back side, and the shared walls are thin, identical to the structure of sponges. As shown in Fig. S6, the pore sizes can be modified by changing the volume of the non-solvent, water, probably due to a change in the solvent exchange rate. At a lower ratio of DI water (from 600 mL to 400 mL), the pores have an increased diameter of around 400 nm on the front side. Less water in the system could result in a slower solvent exchange process, thus producing a relatively less-compact structure. Additionally, the ratio of ZSM-5 to PVDF-HFP can be modulated over a wide range from 0 to 9 : 1 to ensure the integrity of the film. As shown in Fig. S7, the film with a ratio of 9 : 1 still has a porous structure constructed through the stacking of inorganic particles. However, the film loses its bendability with a high concentration of ZSM-5.

Fig. 3a–c displays an overview of the ZSM-5 particles incorporated into the HJ film. As calculated by statistical data, the particles have a relatively uniform size distribution with a diameter of 2.288 ± 0.065 μm. To examine the mechanical strength on the surface on a microscopic basis, approach–retrace tests were conducted *via* atomic force microscopy. A conventional PE film was utilized as a contrast sample in the examination, and its image in Fig. 3d shows a fabric morphology with intertwined fibers. Fig. 3e shows a cubic particle inlayed in the PVDF-HFP matrix, with the same structure as mentioned above. Quantitative nanomechanical mapping tests were implemented in the selected area marked with a red star shown in Fig. 3d and e. Comparatively, the HJ film has a peak force four times higher than the PE film, showing high rigidity to resist the penetration of sodium metal. Additionally, as can be seen from the slope in the repulsion part, the HJ film has an elastic modulus ten times higher than the PE film, which indicates a robust surface. In addition to investigation of its mechanical robustness, tests of the thermal stability and fire resistance of the HJ film are shown in Fig. 3h, i and S8. As shown in Fig. 3h and i, both films can be lit within 0.1s with butane. However, in the case of the PE film, the fire continues once the source of fire is removed, while the fire is self-extinguished and the film maintains its shape after the fire is withdrawn for the HJ film. The self-extinguishing behavior of the HJ film is due to the high concentration of molecular sieves and the existence of the element F. To test the high-temperature stability of our film, two samples, a piece of PE film and HJ film, were placed on a heat conductor, and the temperature was set from room temperature to 300 °C. The PE film tended to deform above 110 °C and melted at 147 °C. Unlike the PE film, the HJ film sustained its shape even at 300 °C, showing superior thermal stability. On a cell basis, a battery with PE as the separator would face issue such as short circuit when exposed to fire or heat.

Quasi-solid-state electrolytes have the ability to confine electrolyte solution *via* swelling with liquids, and thus they have been reported to enhance the stability and alleviate liquid leakage problems of rechargeable batteries. For battery tests, the weight ratio of liquids in the gel electrolytes is 30–40%. Additionally, the conductivity of QSSEs reaches the order of magnitude of liquid electrolytes. As depicted in Fig. 4a, a quasi-solid-state cell was assembled with a piece of a Prussian blue analogue (PBA)-based cathode, QSSE and sodium metal foil. The PBA particles were synthesized as previously reported and have a stacked cubic structure as presented in Fig. S9. The chemical composition was identified as $Na_{1.53}Fe[Fe(CN)_6]$ and the crystal structure was confirmed to be a sodium-deficient cubic phase as previously reported. The Nyquist plots of the

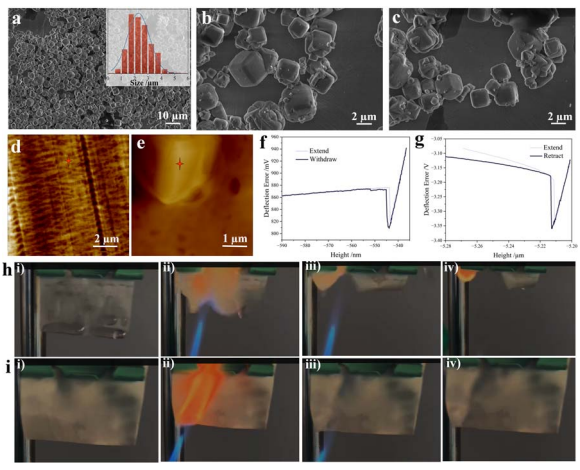

Fig. 3 Robustness of the HJ film. (a–c) SEM images of ZSM-5 particles at different magnifications. Atomic force microscopy images of (d) conventional PE film and (e) HJ film. Approach and retrace examination of (f) conventional PE film and (g) HJ film. Ignition tests of (h) conventional PE film and (i) HJ film with butane.

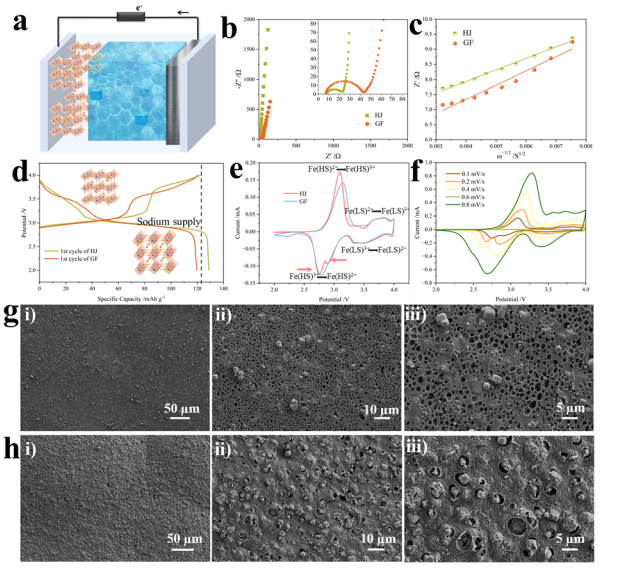

Fig. 4 Characterization of charge transfer and diffusion. (a) Schematic illustration of the mechanism of quasi-solid-state sodium ion batteries. (b) Nyquist plots and (c) corresponding Z' *versus* $\omega^{-1/2}$ plots in the low-frequency region of quasi-solid-state and liquid-state SIBs. (d) Initial charge and discharge curves and (e) CV curves of SIBs with HJ QSSEs and glass fiber. (f) CV curves of SIBs with HJ QSSEs at different scanning rates. SEM images of the surface oriented towards sodium metal (g) before and (h) after charge–discharge cycles.

QSS (HJ) and liquid-state (glass fiber, GF) sodium ion batteries are shown in Fig. 4b for comparison. The contact resistance of the HJ-based sample (7.7 Ω) approaches that of the GF-based one (7.2 Ω), indicating a good interfacial contact between the electrodes and QSSE. Additionally, the charge transfer resistance is reduced from 18.0 Ω to 7.5 Ω thanks to the joint effect of the structural and chemical compositional design. The diffusion resistances of the two samples are characterized by the slopes of the fitting lines in Fig. 4c. Generally, a steeper line suggests a higher resistance. Therefore, the cell with HJ has improved sodium ion transport dynamics compared with the one with GF. The conductivity of the HJ film was calculated to be 7.8×10^{-3} S cm^{-1}. Additionally, the steady-state current measurement and impedance spectra before and after polarization on a sodium metal symmetrical cell are shown in Fig. S10. The current response was obtained with an amplitude of 50 mV, and the transference number of sodium ions was determined to be 0.70.

Cubic phase Na-deficient Fe-based PBAs have been reported to have unstable cycling performance over 200 cycles owing to poor crystallinity. Moreover, the cubic phase with a low concentration of Na cannot be restored after the deintercalation of sodium ions.[31] However, in our case, with the Na-type sieve-embedded HJ gel electrolytes, the number of sodium ions that would intercalate back to the framework of PBAs would be greater than the number deintercalated. As depicted in Fig. 4d, the coulombic efficiency of the initial charge–discharge cycle is more than 100% for the HJ-based sample, and the first discharge capacity reaches 130 mAh g^{-1} at a current density of 0.1C. The discharge platform in the relatively lower potential range is also prolonged compared with that of the GF-based sample. Fig. 4e shows the CV curves of two samples at a scanning rate of 0.1 mV s^{-1}. Based on the distance between the oxidation peak and reduction peak, the polarization was minimized for the HJ-based sample. Redox peaks at a lower potential are responsible for high-spin Fe^{2+}/Fe^{3+} that is connected with N sites and the peaks at a higher potential correlate with low-spin Fe^{2+}/Fe^{3+} that is connected with C sites. As revealed by the distance between the oxidation peaks and reduction peaks of high-spin Fe^{2+}/Fe^{3+}, the HJ-based battery has minimized polarization. The reduction peak in the range of 2.5–4.2 V is also split into two peaks; this phenomenon disappears when the scanning rate is increased to 0.8 mV s^{-1}, as displayed in Fig. 4f. The CV curves maintain their shapes when the scanning rate rises from 0.1 mV s^{-1} to 0.8 mV s^{-1}, indicating an excellent rate performance. To elucidate the role of the HJ film, post-cycling SEM and XPS analyses were performed. Fig. 4g and h compare the anode-side surface of the HJ film before and after cycling at different magnifications. The images reveal significant pore shrinkage and the formation of a dense surface layer after cycling. Furthermore, the additional peak at 288.3 eV in the C 1s spectrum, which was assigned to C=O (Fig. S11), confirmed electrolyte decomposition on the HJ film.

The phase transition process during a charge–discharge cycle of QSSE-based sodium ion batteries was revealed using an *in situ* XRD test (Fig. 5a). The three peaks at 22.8°, 23.0° and 23.5° were attributed to the ZSM-5 in the gel electrolytes. These

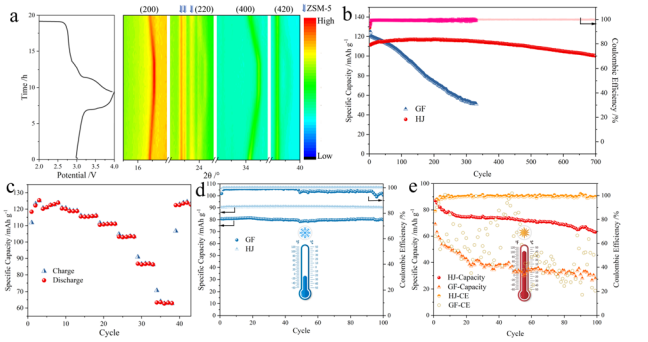

Fig. 5 Stability of the HJ-based quasi-solid-state SIBs at ambient, low and high temperature. (a) *In situ* XRD pattern of PBAs|HJ QSSEs|Na quasi-solid-state SIBs. (b) Comparison of the cycling stability of SIBs with HJ and glass fiber. (c) Rate performance of quasi-solid-state SIBs. 0.1C for three cycles, then 0.2C, 0.3C, 0.5C, 1C, 2C, 5C, 10C and 0.2C for five cycles. Charge–discharge cycles of the quasi-solid-state liquid-state SIBs at (d) −20 °C and (e) 60 °C. The cycling stability tests were all carried out at 1C after activation at 0.1C for three cycles.

three peaks remain in fixed positions, which verified that the molecular sieve ZSM-5 retains its crystal structure, which is mainly constructed by Si and Al, during the charge–discharge procedure. Fig. S12 shows the XRD pattern of the PBA-based cathode; the peaks were identified as reflections from (200), (220), (400) and (420). When the cell was charged, a shift in the peaks towards higher angle was detected at 16.8° and 34.2°, which was assigned to a shortened inter-planar spacing for (200) and (400) for the PBA-based cathode. Additionally, the appearance of an extra line at 24.4°, as well as at 39.2°, indicated that part of the PBA transformed to the rhombohedral phase.[32] The peaks return to their initial positions after discharge back to 2.0 V, implying a reversible phase transformation during a single charge–discharge cycle.

Due to the integrity of its chemical structure, suppressed electrolyte solution corrosion, and stabilized electrolyte–electrode interface, the HJ-based cell exhibits excellent cycling stability over a wide temperature range from −20 °C to 60 °C. The cycling performance at room temperature or over a wide temperature range has been investigated for various polymer electrolytes. Hong Jin Fang *et al.* applied double-layer polymer electrolytes to obtain stable sodium ion batteries with 80.4 mAh g^{-1} capacity after 400 cycles at 1C (room temperature).[33] L. Du *et al.* developed a smart gel polymer electrolyte and applied it to obtain sodium ion batteries with 80% capacity retention after 500 cycles at 50 °C.[34] The cycling performance at 25 °C in the present work is displayed in Fig. 5b. The GF-based cell shows a dramatic capacity drop after 100 charge–discharge cycles, and has a low capacity retention of 43% after 300 cycles, mainly due to the collapse of the crystal structure of PBAs, side reactions in electrolytes, *etc.* The cell experiences a large potential drop during the long-term cycling test, from 0.085 V (1st cycle) to 0.48 V (100th cycle) and 0.76 V (300th cycle), as shown in Fig. S10b. The coulombic efficiency of the GF-based SIB also drifts markedly after 200 cycles, which is owing to side effects and electrolyte exhaustion. For the HJ-gel-based SIB, the

capacity slowly increases for the first 100 cycles, probably due to a sodium ion supply process. The capacity retention is 90% even after 700 cycles, and the coulombic efficiency stays above 99.9% throughout the entire process. Fig. S13a shows that no obvious potential drop occurs after cycling tests. Fig. 5c shows the rate performance at current densities from 0.1C to 10C at ambient temperature. The HJ-based quasi-solid-state SIBs demonstrate outstanding fast sodium ion storage capability, with a capacity of 60 mAh g^{-1} even at a current density of 10C. Polymers are reported to enhance the anti-freezing abilities of liquids. Therefore, the capacity remains 90 mAh g^{-1} for the gel electrolytes, while it drops to 80 mAh g^{-1} for liquid electrolytes at 1C. The potential drops in the charge–discharge curves in Fig. S14 also corroborate the improved conductivity of the gel-based batteries. When the temperature is decreased to −20 °C, both the HJ-based and GF-based cells show high capacity retention of 101% and 99%, respectively, for 100 charge–discharge cycles, as displayed in Fig. 5d. However, after 50 cycles, the coulombic efficiency of the GF-based cells had dropped to around 96%. Sodium dendrites remain troublesome at sub-zero temperature, and they consume a large amount of electrolyte solution. For the HJ-based cell, the coulombic efficiency remains above 99.9%. Liquid electrolytes are intolerant to high temperatures due to solvent evaporation and the acceleration of undesired reactions.[35] As a result, as shown in Fig. 5e, the GF-based SIB exhibits an extremely unstable electrochemical performance at 60 °C, as shown by its coulombic efficiency. The capacity also drops to below 40 mAh g^{-1} after 20 cycles. On the other hand, the coulombic efficiency of the HJ-based SIB remains stable at around 100%, and the capacity retention is 73% after 100 cycles. The charge–discharge curves for the initial and 100th cycle are displayed in Fig. S15. Overall, the HJ-based QSSEs are capable of withstanding temperature variations in the environment.

The thermodynamics and kinetics of the growth of sodium dendrites remain a project requiring further exploration. However, it is commonly recognized that sodium metal has an unstable solid electrolyte interphase, high reactivity with the electrolyte and non-uniform dendrite growth. *Operando* confocal microscopy was thus applied under galvanostatic conditions to observe the dendrite growth for a quasi-solid-state SIB and a liquid-state SIB, as shown in Fig. 6. Observations were conducted at a current density of 0.1C and 1C, and the respective charge–discharge curves are shown in Fig. 6a. Confocal microscopic videos were taken with a view concentrating on the gel electrolyte or glass fiber, as depicted in Fig. 6b.

The evolution through the charge–discharge process is displayed in Fig. S16 *via* screenshots from Video S1. Sodium metal dendrites grew at different positions upon charging to different voltages. When discharged, some parts of sodium metal dendrites would size down and redissolve into sodium ions. The sodium metal dendrites had a moss-like appearance. The sodium metal dendrites at different current densities for the HJ-based quasi-solid-state SIB were compared those of the GF-based liquid-state SIB, and the results are shown in Fig. 6c–e (from Video S1) and Fig. 6f–h (from Video S2). As shown in Fig. 6c–e, the penetration of sodium dendrites when the rate

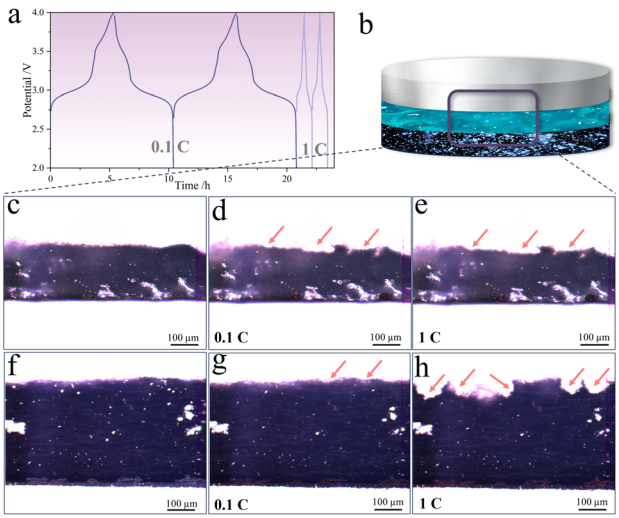

Fig. 6 *Operando* microscopic observation of quasi-solid-state and liquid-state SIBs during operation. (a) Charge and discharge curves of SIBs at different current densities. (b) Schematic illustration of the observation view. Images of the of quasi-solid-state SIBs in the (c) initial and (d) charged state at a current density of 0.1C and the (e) charged state at 1C. Image of the liquid-state SIBs in the (f) initial and (g) charged state at a current density of 0.1C and (h) charged state at 1C.

was increased from 0.1C to 1C was hindered. Therefore, the risk of short circuit and other hazards such as electrolyte consumption, dead sodium, *etc.*, have been minimized. In contrast, the sodium dendrites clearly penetrated deeper into the glass fiber when the rate was increased, as can be seen from Fig. 6f–h. The substantial improvement is partly attributed to the hardness of the surface with abundant ceramic particles. Additionally, the limited amount of electrolyte and the sodiophilic nature of the molecular sieves also contribute to the improved performance.[36]

Conclusions

We have fabricated a quasi-solid-state electrolyte film with a spontaneously formed Janus-faced honeycomb-like structure. Due to the joint effects of the polymer and molecular sieves, the film is flexible, bendable, robust and has high conductivity for sodium ions. When applied to sodium ion batteries, the as-obtained electrolyte demonstrated its superiority in constraining extra liquid solvent and supplying sodium ions. The HJ-based quasi-solid-state SIB achieved excellent performance with long-term cycling stability, with 90% capacity retention and a stable coulombic efficiency of over 99.9% after 700 cycles. The mechanism of the outstanding electrochemical stability was revealed by *in situ* XRD measurements and *operando* confocal microscopic observation. The evidence testified that the PBA-based cathode partially experiences a cubic-to-rhombohedral phase transition; furthermore, the phase transition and crystal structure expansion process are entirely reversible. The growth of sodium dendrites is suppressed, especially at high current density, which contributes to high

safety, high coulombic efficiency, and long cycle life. Moreover, the unique structure design broadened the temperature range to which it can adapt from −20 °C to 60 °C. There is more to explore in terms of these multi-functional QSS electrolytes than has been presented in this paper, and we hope these findings will inspire further research.

Author contributions

Fang Chen: conceptualization, methodology, investigation, data curation, writing—original draft. Yadan Xie: investigation, validation, data curation. Yubin Zhou: investigation, resources, validation. Na Li: resources, formal analysis, validation. Yu Qiao: conceptualization, supervision, writing—review & editing, project administration. Xiang Ding: conceptualization, supervision, funding acquisition, writing—review & editing.

Conflicts of interest

There are no conflicts to declare.

Data availability

The data that support the findings of this study are available from the author, Fang Chen (chenfang01@zjenergy.com.cn), upon reasonable request.

Supplementary information (SI): detailed supporting document (covering structure, physical properties, electrochemical performance, *etc.*) and two *operando* microscopic observation videos. See DOI: https://doi.org/10.1039/d5sc08536e.

Acknowledgements

This work is supported by Department of Science and Technology of Zhejiang Province (grant number 31941023072), the National Natural Science Foundation of China (52102216), the Key Laboratory of Applied Surface and Colloid Chemistry (Shaanxi Normal University), Ministry of Education (2025067), the open project of Anhui Province Key Laboratory of Efficient Conversion and Solid-State Storage of Hydrogen & Electricity (2025KF03), the Key Laboratory of Green Extraction & Efficient Utilization of Light Rare-Earth Resources (Inner Mongolia University of Science & Technology), Ministry of Education (REKF25002), the Anhui Key Laboratory of Nanomaterials and Nanotechnology, the Major Science and Technology Projects in Anhui Province (202305a12020006), the Open Project of State Key Laboratory of Inorganic Synthesis and Preparative Chemistry (2025-22).

References

1 H. Pourzolfaghar, P.-Y. Wang, X.-Y. Jiang, S. Kositsarakhom, W. Jirasupcharoen, C. Suwantri, D. Jyothi, K. Prabhakaran and Y.-Y. Li, Emerging trends and innovations in all-solid-state lithium batteries: A comprehensive review, *Chem. Eng. J.*, 2024, **500**, 157394.

2 Z. Cheng, T. Liu, B. Zhao, F. Shen, H. Jin and X. Han, Recent advances in organic-inorganic composite solid electrolytes for all-solid-state lithium batteries, *Energy Storage Mater.*, 2021, **34**, 388–416.

3 H. Aziam, B. Larhrib, C. Hakim, N. Sabi, H. B. Youcef and I. Saadoune, Solid-state electrolytes for beyond lithium-ion batteries: A review, *Renew. Sustain. Energy Rev.*, 2022, **167**, 112694.

4 J. Lu, Y. Chen, Y. Lei, P. Jaumaux, H. Tian and G. Wang, Quasi-Solid Gel Electrolytes for Alkali Metal Battery Applications, *Nano-Micro Lett.*, 2025, **17**, 1–66.

5 K. Aruchamy, S. Ramasundaram, S. Divya, M. Chandran, K. Yun and T. H. Oh, Gel polymer electrolytes: advancing solid-state batteries for high-performance applications, *Gels*, 2023, **9**, 585.

6 X. Fan, C. Zhong, J. Liu, J. Ding, Y. Deng, X. Han, L. Zhang, W. Hu, D. P. Wilkinson and J. Zhang, Opportunities of flexible and portable electrochemical devices for energy storage: expanding the spotlight onto semi-solid/solid electrolytes, *Chem. Rev.*, 2022, **122**, 17155–17239.

7 P. Jaumaux, J. Wu, D. Shanmukaraj, Y. Wang, D. Zhou, B. Sun, F. Kang, B. Li, M. Armand and G. Wang, Non-flammable liquid and quasi-solid electrolytes toward highly-safe alkali metal-based batteries, *Adv. Funct. Mater.*, 2021, **31**, 2008644.

8 H. Huo and J. Janek, Solid-state batteries: from 'all-solid'to 'almost-solid', *Natl. Sci. Rev.*, 2023, **10**, nwad098.

9 L. Mazzapioda, A. Tsurumaki, G. Di Donato, H. Adenusi, M. A. Navarra and S. Passerini, Quasi-solid-state electrolytes-strategy towards stabilising Li| inorganic solid electrolyte interfaces in solid-state Li metal batteries, *Sol. Energy Mater.*, 2023, **3**, 1–3025.

10 J. Chattopadhyay, T. S. Pathak and D. M. Santos, Applications of polymer electrolytes in lithium-ion batteries: A review, *Polymers*, 2023, **15**, 3907.

11 D. Zhou, D. Shanmukaraj, A. Tkacheva, M. Armand and G. Wang, Polymer electrolytes for lithium-based batteries: advances and prospects, *Chem*, 2019, **5**, 2326–2352.

12 J. Zheng, W. Li, X. Liu, J. Zhang, X. Feng and W. Chen, Progress in gel polymer electrolytes for sodium-ion batteries, *Energy Environ. Mater.*, 2023, **6**, e12422.

13 F. Gebert, J. Knott, R. Gorkin III, S.-L. Chou and S.-X. Dou, Polymer electrolytes for sodium-ion batteries, *Energy Storage Mater.*, 2021, **36**, 10–30.

14 Z. Chang, H. Yang, X. Zhu, P. He and H. Zhou, A stable quasi-solid electrolyte improves the safe operation of highly efficient lithium-metal pouch cells in harsh environments, *Nat. Commun.*, 2022, **13**, 1510.

15 Y. Gao, H. Zhang, J. Peng, L. Li, Y. Xiao, L. Li, Y. Liu, Y. Qiao and S. L. Chou, A 30-year overview of sodium-ion batteries, *Carbon Energy*, 2024, **6**, e464.

16 P. K. Nayak, L. Yang, W. Brehm and P. Adelhelm, From lithium-ion to sodium-ion batteries: advantages, challenges, and surprises, *Angew. Chem., Int. Ed.*, 2018, **57**, 102–120.

17 F. Huang, P. Xu, G. Fang and S. Liang, In-depth understanding of interfacial Na+ behaviors in sodium

metal anode: migration, desolvation, and deposition, *Adv. Mater.*, 2024, **36**, 2405310.
18 Y.-S. Hong, N. Li, H. Chen, P. Wang, W.-L. Song and D. Fang, In operando observation of chemical and mechanical stability of Li and Na dendrites under quasi-zero electrochemical field, *Energy Storage Mater.*, 2018, **11**, 118–126.
19 A. Rudola, D. Aurbach and P. Balaya, A new phenomenon in sodium batteries: Voltage step due to solvent interaction, *Electrochem. Commun.*, 2014, **46**, 56–59.
20 B. Yadav, C. B. Soni, S. Bera, H. Kumar and V. Kumar, Direct observation of sodium dendrites to decipher the complicated behavior of electrolyte systems, *Electrochim. Acta*, 2024, **507**, 145212.
21 B. Lee, E. Paek, D. Mitlin and S. W. Lee, Sodium metal anodes: emerging solutions to dendrite growth, *Chem. Rev.*, 2019, **119**, 5416–5460.
22 H. Wang, E. Matios, J. Luo and W. Li, Combining theories and experiments to understand the sodium nucleation behavior towards safe sodium metal batteries, *Chem. Soc. Rev.*, 2020, **49**, 3783–3805.
23 T. Wang, Y. Hua, Z. Xu and J. S. Yu, Recent advanced development of artificial interphase engineering for stable sodium metal anodes, *Small*, 2022, **18**, 2102250.
24 W. Wang, Y. Gang, Z. Hu, Z. Yan, W. Li, Y. Li, Q.-F. Gu, Z. Wang, S.-L. Chou and H.-K. Liu, Reversible structural evolution of sodium-rich rhombohedral Prussian blue for sodium-ion batteries, *Nat. Commun.*, 2020, **11**, 980.
25 J. Peng, W. Zhang, Q. Liu, J. Wang, S. Chou, H. Liu and S. Dou, Prussian blue analogues for sodium-ion batteries: past, present, and future, *Adv. Mater.*, 2022, **34**, 2108384.
26 S. Fan, Y. Liu, Y. Gao, Y. Liu, Y. Qiao, L. Li and S. L. Chou, The design and synthesis of Prussian blue analogs as a sustainable cathode for sodium-ion batteries, *SusMat*, 2023, **3**, 749–780.
27 M.-C. Long, G. Wu, X.-L. Wang and Y.-Z. Wang, *Energy Storage Mater.*, 2022, **53**, 62–71.
28 X. Mu, X. Li, C. Liao, H. Yu, Y. Jin, B. Yu, L. Han, L. Chen, Y. Kan and L. Song, *Adv. Funct. Mater.*, 2022, **32**, 2203006.
29 F. Chen and C. Chen, Spontaneously formed ant-nest structure for binder-free sodium ion batteries with ultra-high electrode loading, *Chem. Eng. J.*, 2023, **466**, 143327.
30 S. Zhou, Y. Yang, L. Shi, S. Zhang, J. Wang, F. Zhang and S. Zhao, Recent progress of gel-based materials in energy storage and conversion, *Mater. Horiz.*, 2025, **12**(17), 6650–6680.
31 W.-J. Li, S.-L. Chou, J.-Z. Wang, Y.-M. Kang, J.-L. Wang, Y. Liu, Q.-F. Gu, H.-K. Liu and S.-X. Dou, Facile method to synthesize Na-enriched Na1+ x FeFe (CN) 6 frameworks as cathode with superior electrochemical performance for sodium-ion batteries, *Chem. Mater.*, 2015, **27**, 1997–2003.
32 H. Zhang, J. Li, J. Liu, Y. Gao, Y. Fan, X. Liu, C. Guo, H. Liu, X. Chen and X. Wu, Understanding capacity fading from structural degradation in Prussian blue analogues for wide-temperature sodium-ion cylindrical battery, *Nat. Commun.*, 2025, **16**, 2520.
33 J. Pan, Y. Zhang, F. Sun, M. Osenberg, A. Hilger, I. Manke, R. Cao, S. X. Dou and H. J. Fan, *Angew. Chem., Int. Ed.*, 2023, **62**, e202219000.
34 L. Du, G. Xu, C. Sun, Y.-H. Zhang, H. Zhang, T. Dong, L. Huang, J. Ma, F. Sun and C. Li, *Nat. Commun.*, 2025, **16**, 2979.
35 X. Zhou, Y. Zhou, L. Yu, L. Qi, K.-S. Oh, P. Hu, S.-Y. Lee and C. Chen, Gel polymer electrolytes for rechargeable batteries toward wide-temperature applications, *Chem. Soc. Rev.*, 2024, **53**, 5291–5337.
36 W. Tang, R. Qi, J. Wu, Y. Zuo, Y. Shi, R. Liu, W. Yan and J. Zhang, Engineering, understanding, and optimizing electrolyte/anode interfaces for all-solid-state sodium batteries, *Electrochem. Energy Rev.*, 2024, **7**, 23.